Electronic Supplementary Material (ESI) for Nanoscale.
This journal is © The Royal Society of Chemistry 2019

# Supporting Information

# Kinetics, Energetics, and Size Dependence of the Transformation from Pt to Ordered PtSn Intermetallic Nanoparticles

*Minda Chen,[1] Yong Han,[2] Tian Wei Goh,[1] Rong Sun,[1,3] Raghu V. Maligal-Ganesh,[1] Yuchen Pei,[1] Chia-Kuang Tsung,[4] James W. Evans,*,[2,5] Wenyu Huang*,[1,5]*

[1]Department of Chemistry, Iowa State University, Ames, Iowa 50011, United States

[2]Department of Physics and Astronomy, Iowa State University, Ames, Iowa 50011, United States

[3]Department of Chemistry, Beijing Normal University, Beijing, China

[4]Department of Chemistry, Boston College, Chestnut Hill, MA 02467, United States

[5]Division of Chemical and Biological Sciences, Ames Laboratory, U.S. Department of Energy, Ames, Iowa 50011, United States

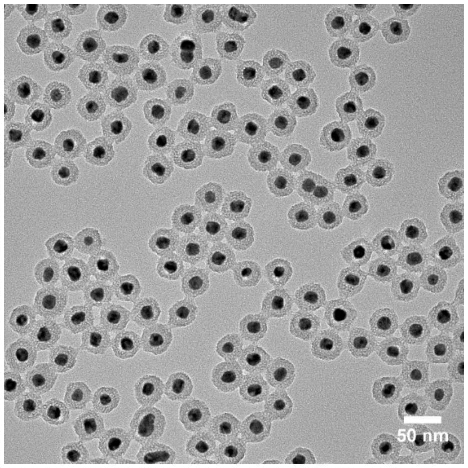

**Figure S1.** TEM image of 14 nm Pt@$mSiO_2$ NPs after 120 min transformation at 260 °C.

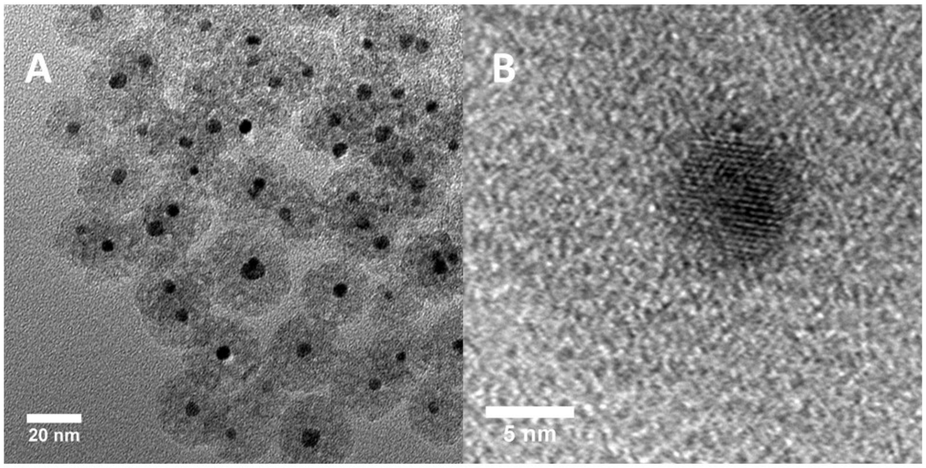

**Figure S2.** (A) TEM and (B) HR-TEM image of 5 nm Pt@$mSiO_2$ NPs after 120 min transformation at 250 °C. Lattice spacing in (B) is 0.294 nm and matches PtSn(101).

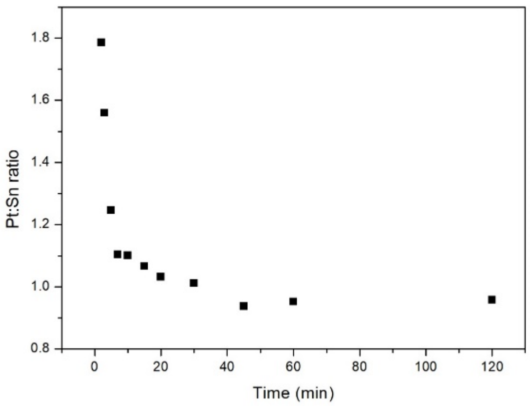

**Figure S3.** ICP-MS measurement of Pt:Sn ratio in the Pt/PtSn@mSiO$_2$ samples from 14 nm, 240°C experiment**.**

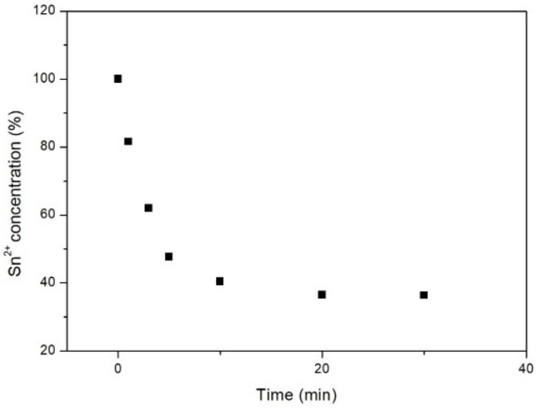

**Figure S4.** ICP-MS measurement of $Sn^{2+}$ concentration in the solution after removal of Pt/PtSn@mSiO$_2$. Samples are from 14 nm, 240°C experiment.

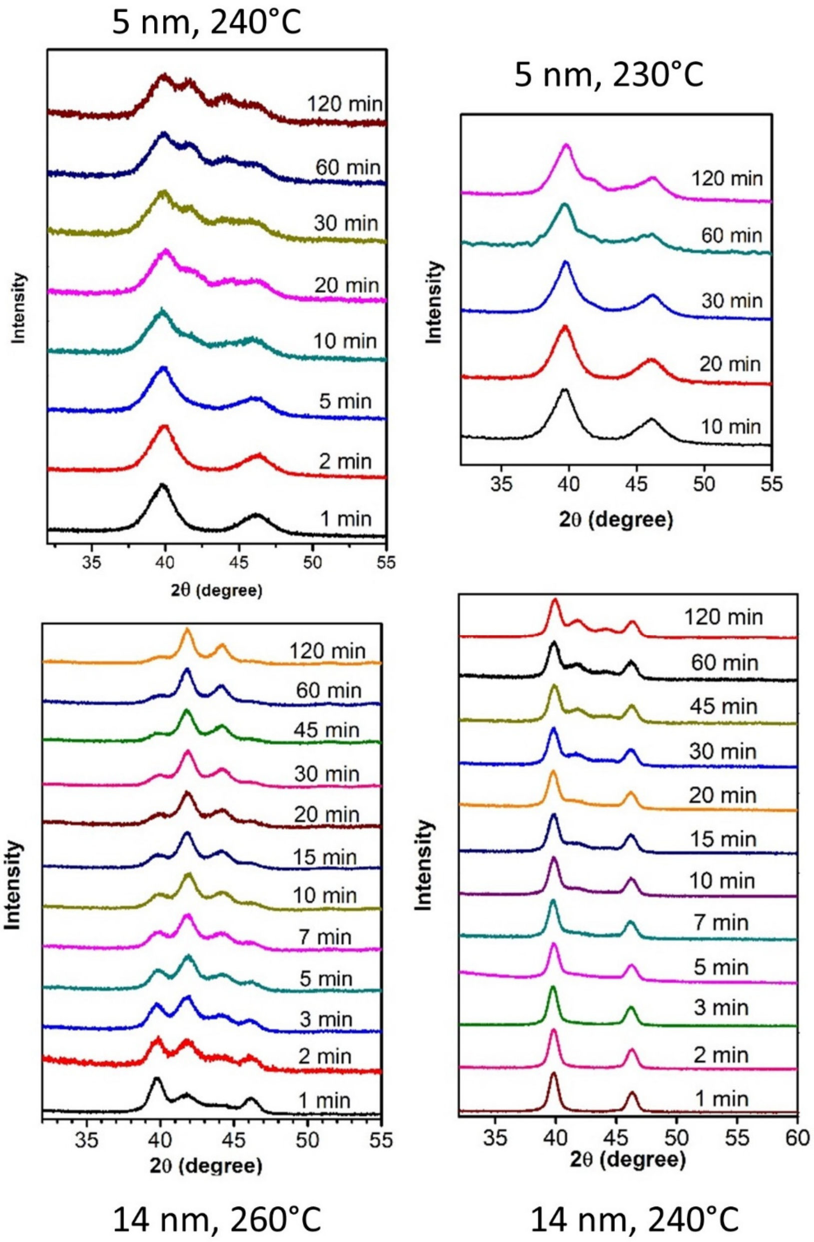
5 nm, 240°C

5 nm, 230°C

14 nm, 260°C

14 nm, 240°C

**Figure S5.** Time-evolution XRD patterns of (A) 5 and (B) 14 nm Pt@m$SiO_2$ transformed to PtSn@m$SiO_2$ at various designated temperatures.

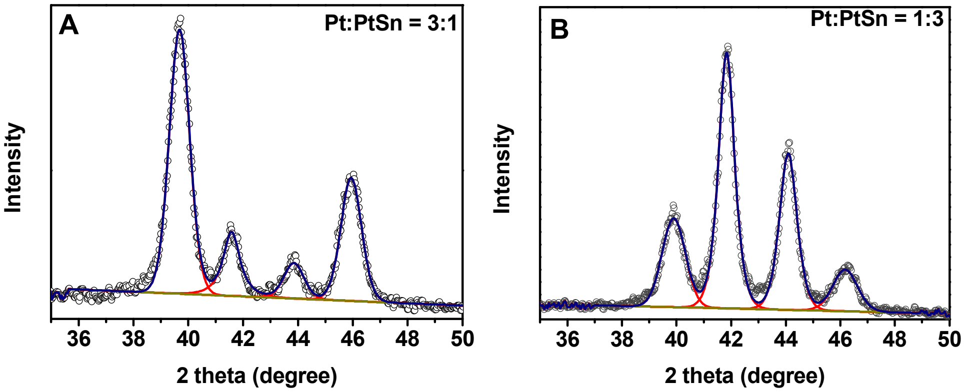

**Figure S6.** XRD pattern of (A) 3:1 and (B) 1:3 standard mixture of Pt and PtSn and their deconvolution. The black circles representing XRD raw data, the red lines representing each deconvoluted peaks, the dark yellow line representing a linear baseline, and the dark blue line representing the sum of all deconvoluted peaks.

## The effect of mesoporous silica shell

In designing heterogeneous catalysts, inorganic supports like silica, alumina or titania are generally utilized to disperse and stabilize the metal catalyst.[1] Our mesoporous silica shell is an improved extension of those supports, customized to provide further advantages as that:

1. Silica is chemically and thermodynamically inert. It makes the mesoporous silica shell stable at various synthesis or catalysis conditions.
2. Mesopores within the silica shell provide uninhibited access from the chemical environment to the metal core (discussed in detail below).
3. The core-shell structure enables us to achieve high metal loading without worrying about nanoparticle aggregation, which benefits further catalysis.
4. Our Pt@mSiO$_2$ and PtSn@mSiO2 nanoparticles better mimic typical realistic catalytic systems (metal NPs on extended oxide supports) than surfactant-coated NPs.

In our previous work,[2] we have extensively studied the seeded growth mechanism in the silica shell and we found that the silica shell is etched by inorganic salts during the intermetallic synthesis, which provides sufficient space for the expansion of metal core. Additionally, by measuring the metal core diameter and silica shell thickness of the Pt nanoparticles in Figure 1(A), we obtained a Pt core size of 13.8 ± 1.4 nm and a silica shell thickness of 14.1 ± 0.8 nm. By measuring the nanoparticles after conversion in Figure S1, we confirm that the metal core grew to 19.1 ± 1.1 nm and the silica shell thickness decreased to 8.9 ± 1.0 nm. This indicates that the mesoporous silica shell did not block the Pt core growth. Other useful data of the silica shell is provided in the table below:

| | thickness (nm) | pore diameter (nm) | pore volume (cm$^3$/g) |
|---|---|---|---|
| 5 nm Pt@mSiO$_2$ | 14.1 ± 0.8 | 2.1 | 0.57 |
| 14 nm Pt@mSiO$_2$ | 9.1 ± 1.0 | 2.5 | 0.58 |

Besides, those mesoporous silica shell should be treated with no difference from general inorganic supports. By using those Pt@mSiO$_2$ nanoparticles, we were trying to adapt to a more “realistic” condition that’s close to general catalyst designing. To illustrate that, we employed another support material, where 5 nm Pt nanoparticles are made and deposited onto 100 nm silica spheres (method follows previous literature[3]). In this case, those silica spheres are surface functionalized with NH$_2$ group to improve dispersion the Pt nanoparticle, and those Pt nanoparticles have uninhibited contact with the chemical environment. We performed the conversion to PtSn at 250 °C, expecting that the results will repeat the previous experiment with the 5 nm Pt@mSiO$_2$. Figure S7 below shows the PXRD patterns of samples at various time during the conversion, and their conversion compared to the 5 nm Pt@mSiO$_2$. We notice that there is no significant difference between the two types of materials. Therefore, our mesoporous silica shell has no effect inhibiting NP growth during conversion relative to NPs supported in the exterior surface of common inorganic support materials.

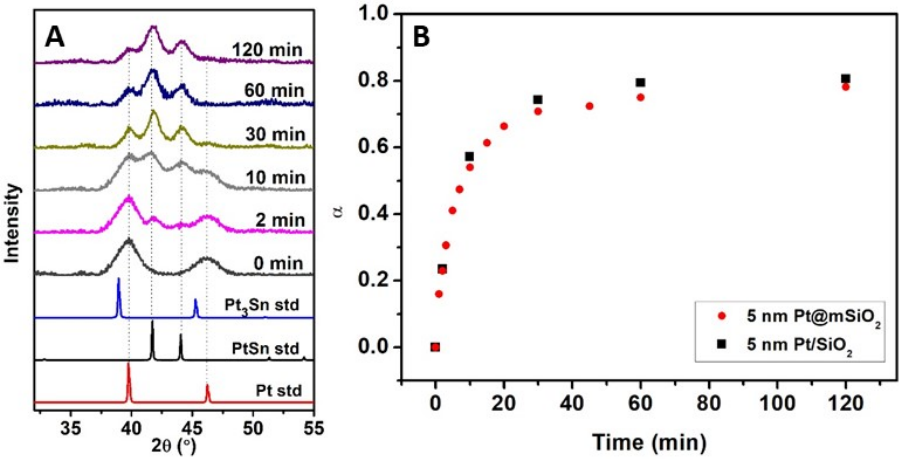

**Figure S7** (A) Time-evolution PXRD patterns of 5 nm Pt/SiO$_2$ converting to PtSn at 250 °C and (B) the corresponding conversion compared to 5 nm Pt@mSiO$_2$.

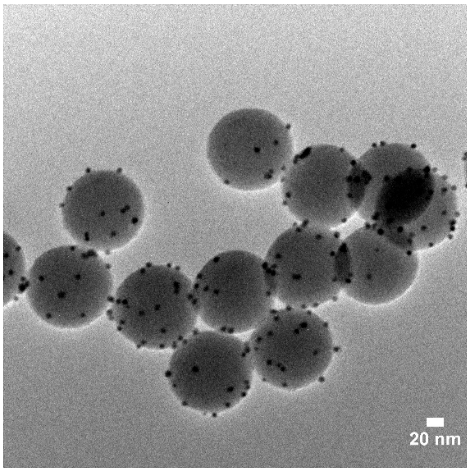

**Figure S8.** TEM image of 5 nm Pt/SiO$_2$ after 120 min transformation at 250 °C. The dominate phase is PtSn as shown by the XRD in Figure S7A.

Previous literature observed the intermetallic nanoparticle growth with organic surfactants to stabilize the nanoparticles during synthesis.[4, 5] Although the study generates valuable insights, it also introduces further complexities regarding the interaction between the organic surfactants and the metal nanoparticle, in terms of the surfactants density on the metal surface and, the extent to which the strongly bound surfactants affect the kinetics of intermetallic PtSn formation at the surface of the nanoparticles. Moreover, such organic surfactants are known to diminish or inhibit the catalytic activities of metal nanoparticles, therefore making them less desirable from a catalytic perspective.

We have performed a control experiment, however, to observe the Pt to PtSn transformation with 14-nm Pt nanoparticles stabilized by organic surfactants (TTAB, myristyltrimethylammonium bromide). The experiment was performed in the same way as described in the manuscript, with a target temperature of 240 °C. However, we started to observe severe aggregation of the Pt nanoparticles before the reaction mixture reaching 240 °C and the addition of SnCl$_2$ into it. As seen in Figure S9 (A) below, XRD of the precipitated Pt shows a crystal domain size of 19.0 nm. Compared to the crystal domain size of 11.2 nm before heating to 240 °C, it suggests the Pt nanoparticles aggregated despite the surfactant. TEM image of the precipitation, as shown below as Figure S9 (B), confirmed Pt aggregation. This also indicates that an inorganic support material like our mesoporous silica shell is crucial for the synthesis of these intermetallic nanoparticles. Previous literature also shows similar results.[1]

Another control experiment mentioned in the manuscript attempted to reduce Sn precursor without Pt@mSiO$_2$. It was performed by dissolving 0.205 mmol of SnCl$_2$ in tetraethylene glycol, and the flask was heated to 280 °C on a heating mantle. The resulting solution was centrifuged, and no reduced Sn precipitation is observed.

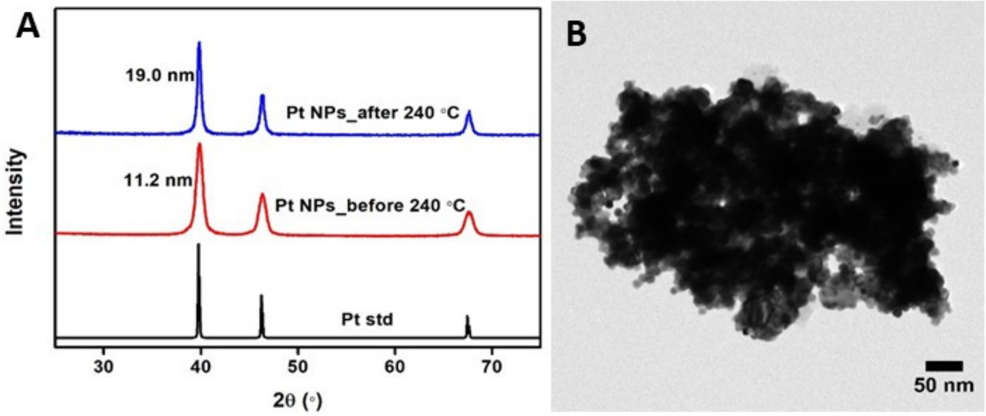

**Figure S9** (A) PXRD patterns of TTAB-capped Pt nanoparticles (B) TEM image of TTAB-capped Pt nanoparticles after heated to 240 °C

### Kinetics for the surface stage of intermetallic formation

We describe a general formulation of kinetics for the first surface stage of intermetallic formation. We assume that the fraction of the Pt NP surface which is not converted to intermetallic as given by $\alpha_{surf} - \alpha$, where again $\alpha_{surf}$ denotes the value of the conversion, $\alpha$, at the end of this stage. We also let $\beta$ denote the fraction of the NP surface which is covered by reduced Sn, and which is also on the portion of the NP surface which is not converted to intermetallic. We regard intermixing on this unconverted portion of the surface as being enhanced relative to any Sn reduced on the intermetallic potions. Finally, $\alpha_{surf} - \alpha - \beta$ gives the fraction of the surface corresponding to exposed Pt. We regard the reduction of Sn as being enhanced on this portion of the NP surface. See Figure S10.

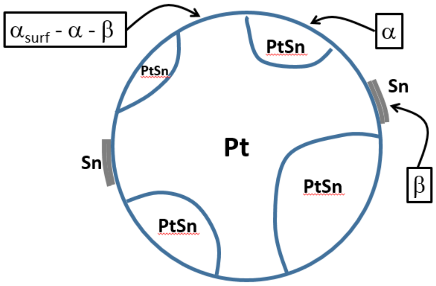

**Figure S10**. Geometry associated with the model for the first surface stage.

We assume reduction requires $m_1$ Pt surface atoms, and that intermixing requires $m_2$ unconverted Pt surface atoms. Then, a mean-Field Langmuirian formulation would suggest the rate equations

$$\frac{\partial}{\partial t}\beta = K_{red}(\alpha_{surf} - \alpha - \beta)^{m_1} - \frac{\partial}{\partial t}\alpha \text{ and} \qquad \text{(S10.1)}$$

$$\frac{\partial}{\partial t}\alpha = K_{mix}\beta(\alpha_{surf} - \alpha)^{m_2} \qquad \text{(S10.2)}$$

Implicitly, these forms assume a random distribution of surface sites converted to intermetallic, and of sites not converted by reduced Sn. Non-randomness in the form of clustering would reduce the exponents. $K_{red}$ and $K_{mix}$ correspond to rates for reduction and intermixing, respectively. We just consider two extreme regimes. If intermixing is facile so that $K_{mix} >> K_{red}$, then one has $\beta \approx 0$ and $d/dt\, \beta \approx 0$, which in turn implies that

$$\frac{\partial}{\partial t}\alpha \approx K_{red}(\alpha_{surf} - \alpha)^{m_1} \text{ so that } m_s = m_1. \qquad \text{(S10.3)}$$

If the reduction is facile so that $K_{red} >> K_{mix}$, then one has $\beta \approx \alpha_{surf} - \alpha$, which in turn implies that

$$\frac{\partial}{\partial t}\alpha = K_{mix}(\alpha_{surf} - \alpha)^{m_2+1}, \text{ so that } m_s = 1+m_2 \qquad \text{(S10.4)}$$

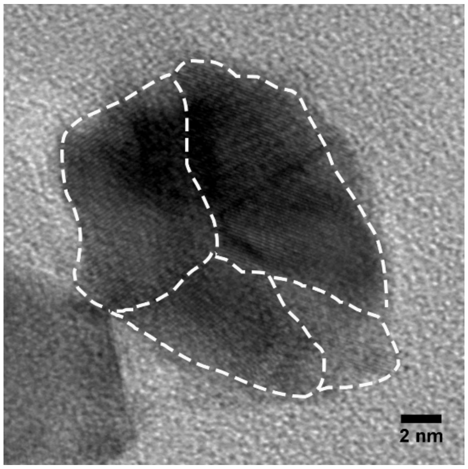

**Figure S11.** HR-TEM image of 14 nm Pt@mSiO$_2$ that shows multiple Pt domains.

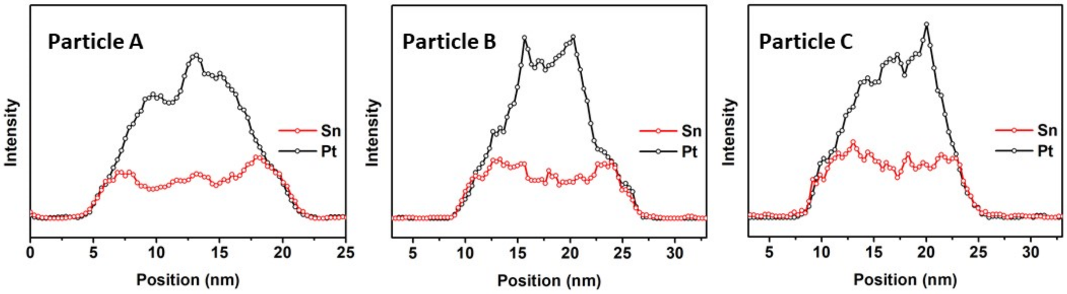

**Figure S12**. Addition EDX line scans on different particles of 14 nm NP after 15 min conversion at 240 °C, when $\alpha = 0.36$.

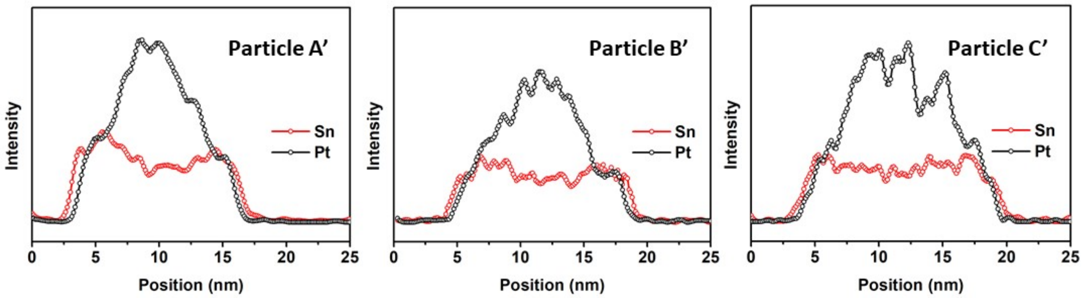

**Figure S13**. Addition EDX line scans on different particles of 14 nm NP after 30 min conversion at 260 °C, when $\alpha = 0.80$.

### Refined Ginstlung-Brounshtein (G-B) formulation

We assume that G-B theory applies only for times $t \geq t_0$ around 20-30 min depending on temperature (T) after which a complete intermetallic PtSn shell of fairly uniform thickness has formed. (This complete PtSn shell will generally be surrounded by a complete Sn shell.) The G-B model assumes a spherical geometry for the NP and analyzes quasi-steady-state diffusion through the shell assuming a source of finite concentration at the outer surface and a sink corresponding to zero concentration at the inner surface. See Figure S14. We solve this G-B model with “initial” conditions at “initial” time $t = t_0$ where $\alpha = \alpha_0$ (between ~0.4 and ~0.8 depending on T). The non-zero “initial” thickness of the intermetallic shell means that its thickness increases at a finite rate at $t_0$. This contrasts the standard G-B model with initial conditions imposed at $t = 0$ where the infinitesimally thin shell means an infinitely large flux across the shell, and thus an infinite growth rate just at $t = 0$.

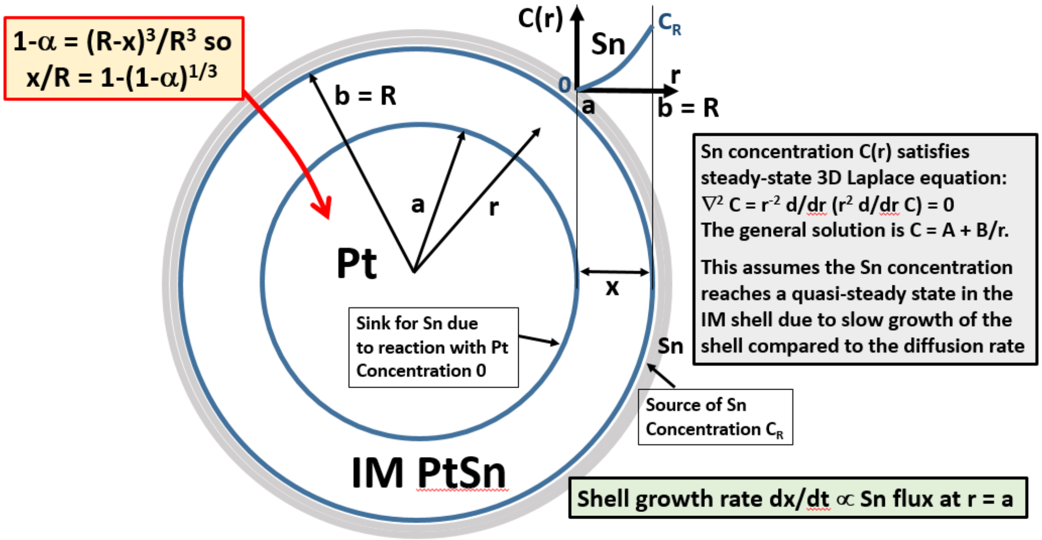

Sn concentration C(r) satisfies steady-state 3D Laplace equation: $\nabla^2 C = r^{-2}\, d/dr\, (r^2\, d/dr\, C) = 0$
The general solution is $C = A + B/r$.

This assumes the Sn concentration reaches a quasi-steady state in the IM shell due to slow growth of the shell compared to the diffusion rate

Sink for Sn due to reaction with Pt Concentration 0

Source of Sn Concentration $C_R$

**Figure S14** Schematic of our refined G-B model

Solution of the steady-state diffusion equation in the shell yields $C(r) = bC_R(r - a)/(rb - ra)$ where CR is the concentration at the outer surface r = b = R.[6] This leads to a diffusion flux $\frac{\partial C}{\partial r} = RC_R/[(R - x)x]$ at r = a, and thus an evolution equation for shell thickness.[6]

$$\frac{\partial}{\partial t}x = \frac{kR}{Rx - x^2}, \tag{S14.2}$$

where k is proportional to the diffusion coefficient. We now rearrange and integrate (S10.2) with the appropriate initial conditions x = $x_0$ and t = $t_0$. Setting u = x/R, so that du/dt = $kR^{-2}/(u - u^2)$, leads to the result

$$\frac{1}{2}(u^2 - {u_0}^2) - \frac{1}{3}(u^3 - {u_0}^3) = kR^{-2}(t - t_0), \tag{S14.3}$$

where $u_0 = x_0/R$ and $u_0 = 1 - (1-\alpha_0)^{1/3}$.

Then, one substitutes $u = 1 - (1-\alpha)^{1/3}$ into (S14.3) to obtain

$$\frac{1}{2}\left[1 - (1 - \alpha)^{\frac{1}{3}}\right]^2 - \frac{1}{3}\left[1 - (1 - \alpha)^{\frac{1}{3}}\right]^3 = kR^{-2}(t - t_0) + \frac{{u_0}^2}{2} - \frac{{u_0}^3}{3} = kR^{-2}(t + t^*), \tag{S14.4}$$

where $t^* = -t_0 + R^2/(2k)\, {u_0}^2 - R^2/(3k)\, {u_0}^3$ (= 0 in the standard GB theory with $t_0 = x_0 = 0$). The left-hand-side of (S14.4) can be simplified to ½ $[1 - (2/3)\alpha - (1-\alpha)^{2/3}]$ which leads to the result

$$1 - \frac{2}{3}\alpha - (1 - \alpha)^{\frac{2}{3}} = K(t + t^*) \text{ where } K = 2kR^{-2}. \tag{S14.5}$$

Since data corresponding to the diffusion stage is limited, and since the variation of α in this stage is limited, there is substantial uncertainty in the determination of $K_d$ and the associated $E_{ad}$. Data fitting using the approach described above based on the last 4 data points is shown in Figure 4B. This analysis yields $K_d = 2.77*10^{-4}$ and t* = 410 min at 260 °C, $K_d = 2.06*10^{-4}$ and t* = 400 min at 250 °C, and $K_d = 0.60*10^{-4}$ and t* = 417 min at 240 °C The associated activation barrier is $E_{ad} \approx 175$ kJ/mol, as seen in figure S15. However, there is substantial uncertainty of about ± 60 kJ/mol.

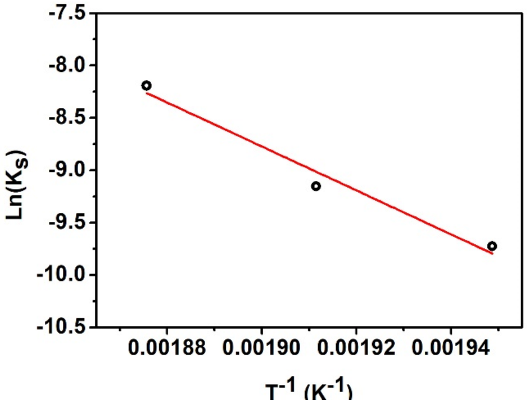

**Figure S15.** Arrhenius plot for diffusion stage of 14 nm Pt NPs.

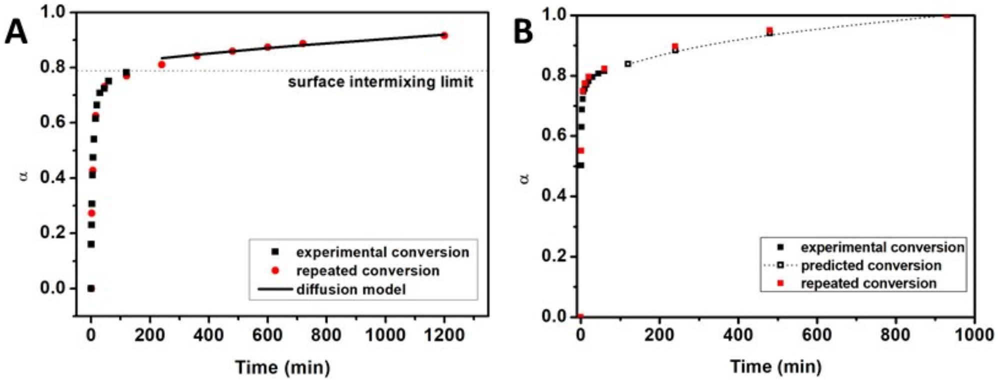

**Figure S16**. Control experiments that extended the reaction time for converting (A) 5 nm Pt@mSiO$_2$ at 250 °C and (B) 14 nm Pt@mSiO$_2$ at 260 °C.

## DFT benchmark analyses for the Pt-Sn systems

In the tables below, we listed the k mesh and energy cutoff Ecut used in our DFT calculation for each bulk system. The cohesive energy for a single-element system is calculated as $E_{\mathrm{c}} = E_{\mathrm{bulk}}/N - E_{\mathrm{one}}$, where $E_{\mathrm{bulk}}$ is the total energy of a primitive cell, N is the number of atoms in a primitive cell, and $E_{\mathrm{one}}$ is the energy of one atom in gas phase.

**Table S17** Lattice constant *a* and cohesive energy $E_c$ from different density functionals for bulk Pt (fcc structure). Experimental values are listed as a comparison (RT denotes "room temperature").

| Method | **k** mesh | $E_{cut}$ (eV) | *a* (nm) | $E_c$ (eV/atom) |
|---|---|---|---|---|
| PBE | 61 × 61 × 61 | 400.000 | 0.3968 | 5.489 |
| PBEsol | 61 × 61 × 61 | 400.000 | 0.3916 | 6.405 |
| optB88 | 61 × 61 × 61 | 400.000 | 0.3979 | 5.818 |
| optB88 | 61 × 61 × 61 | 600.000 | 0.3980 | 5.819 |
| Experiment[7] | | | 0.392 at RT | 5.84 |
| Experiment[8] | | | 0.39160 at 0 K | |

**Table S18** Lattice constant *a* and cohesive energy $E_c$ from different density functionals for bulk $\alpha$-Sn (diamond structure). Experimental values are listed as a comparison.

| Method | **k** mesh | $E_{cut}$ (eV) | *a* (nm) | $E_c$ (eV/atom) |
|---|---|---|---|---|
| PBE | 61 × 61 × 61 | 300.000 | 0.6653 | |
| PBE | 61 × 61 × 61 | 400.000 | 0.6654 | 3.191 |
| PBEsol | 61 × 61 × 61 | 300.000 | 0.6544 | |
| PBEsol | 61 × 61 × 61 | 400.000 | 0.6543 | 3.561 |
| Experiment[7] | | | 0.649 at RT | 3.14 |
| Experiment[9] | | | 0.64912 at RT | |
| Experiment[10] | | | 0.64892 at 295.15 K | |

**Table S19** Lattice constants (*a* and *c*) and cohesive energy $E_c$ from different density functionals for bulk $\beta$-Sn (tetragonal structure). Experimental values are listed as a comparison.

| Method | **k** mesh | $E_{cut}$ (eV) | *a* and *c* (nm) | $E_c$ (eV/atom) |
|---|---|---|---|---|
| PBE | 61 × 61 × 61 | 400.000 | *a* = 0.5942<br>*c* = 0.3212 | 3.153 |
| PBEsol | 61 × 61 × 61 | 400.000 | *a* = 0.5840<br>*c* = 0.3156 | 3.594 |
| Experiment[11] | | | *a* = 0.58312<br>*c* = 0.31814 at 298.15 K | |
| Experiment[12] | | | *a* = 0.58318<br>*c* = 0.31819 at 298.15 K | |

**Table S20** Lattice constant *a* from different density functionals for bulk $Pt_3Sn$ ($Cu_3Au$ structure). Experimental values are listed as a comparison.

| Method | **k** mesh | $E_{cut}$ (eV) | *a* (nm) |
|---|---|---|---|
| PBE | 61 × 61 × 61 | 400.000 | 0.4057 |
| PBEsol | 61 × 61 × 61 | 400.000 | 0.4005 |
| Experiment[13] | | | 0.400 |
| Experiment[14] | | | 0.4004 |

**Table S21** Lattice constants *a* and *c* from different density functionals for bulk PtSn (NiAs structure). Experimental values are listed as a comparison.

| Method | **k** mesh | $E_{cut}$ (eV) | *a* and *c* (nm) |
|---|---|---|---|
| PBE | 61 × 61 × 61 | 400.000 | $a = 0.4176$<br>$c = 0.5508$ |
| PBEsol | 61 × 61 × 61 | 400.000 | $a = 0.4119$<br>$c = 0.5437$ |
| Experiment[14] | | | $a = 0.4108$<br>$c = 0.5450$ |

**Table S22** The DFT energy (eV) per unit cell of bulk $Pt_3Sn$ and PtSn relative to bulk Pt and Sn.

| Method | Pt and $\alpha$-Sn → $Pt_3Sn$ | Pt and $\beta$-Sn → $Pt_3Sn$ | Pt and $\alpha$-Sn → PtSn | Pt and $\beta$-Sn → PtSn |
|---|---|---|---|---|
| PBE | -1.538 | -1.576 | -2.346 | -2.423 |
| PBEsol | -1.673 | -1.640 | -2.491 | -2.425 |

### Demonstration of the stability of a thin PtSn alloy layer at the surface of bulk Pt

Although we have confirmed the stability of bulk Pt-Sn alloys, it is appropriate to investigate the stability of surface alloys, i.e., alloys formed by conversion of a limited number of near-surface layers of the Pt NPs by addition of one or more layers of Sn to the surface. In the initial stages of the process with limited Sn and a substantial excess of Pt, it is reasonable to anticipate the formation of a near-surface fcc $Pt_3Sn$-type alloy which includes alternating (100) layers of c(2 × 2) Pt-Sn and of pure Pt. This picture motivates our comparison of the energies of: (i) a Sn single-atom layer on Pt(100); and (ii) a top first single-atom layer and a lower third single-atom layer both with c(2 × 2) Pt-Sn structure, and a second and fourth and lower single-atom layers of pure Pt. The energy per lateral 2 × 2 unit cell is lowered by -3.60 eV, so such surface alloy formation is thermodynamically favorable. We note that, in this analysis, the Sn adlayer with alternating Sn heights in a c(2 × 2) pattern has lower energy than an adlayer with equal height Sn, and the surface alloy configuration described with a Pt-Sn surface termination has lower energy than the configuration with a Pt termination. The analogous comparison with two surface Sn single-atom layers converting to four c$(2 \times 2)$ Pt-Sn layers including the top single-atom layer, and with interspersed with pure Pt single-atom layers, reveals that the energy is lowered by -10.49 eV per $2 \times 2$ cell. This further supports the thermodynamic favorability of PtSn surface alloy formation.

**Reference:**

1. Bauer, J. C.; Chen, X.; Liu, Q.; Phan, T.-H.; Schaak, R. E., Converting nanocrystalline metals into alloys and intermetallic compounds for applications in catalysis. *J. Mater. Chem.* **2008**, *18*, 275-282.
2. Pei, Y.; Maligal-Ganesh, R. V.; Xiao, C.; Goh, T.-W.; Brashler, K.; Gustafson, J. A.; Huang, W., An inorganic capping strategy for the seeded growth of versatile bimetallic nanostructures. *Nanoscale* **2015**, *7*, 16721-16728.
3. Dong, B.; Pei, Y.; Zhao, F.; Goh, T. W.; Qi, Z.; Xiao, C.; Chen, K.; Huang, W.; Fang, N., In situ quantitative single-molecule study of dynamic catalytic processes in nanoconfinement. *Nat. Catal.* **2018**, *1*, 135-140.
4. Wu, L.; Fournier, A. P.; Willis, J. J.; Cargnello, M.; Tassone, C. J., In Situ X-ray Scattering Guides the Synthesis of Uniform PtSn Nanocrystals. *Nano Lett.* **2018**, *18*, 4053-4057.
5. Wang, C. Y.; Chen, D. P.; Sang, X. H.; Unocic, R. R.; Skrabalak, S. E., Size-Dependent Disorder-Order Transformation in the Synthesis of Monodisperse Intermetallic PdCu Nanocatalysts. *ACS Nano* **2016**, *10*, 6345-6353.
6. Khawam, A.; Flanagan, D. R., Solid-state kinetic models: Basics and mathematical fundamentals. *J. Phys. Chem. B* **2006**, *110*, 17315-17328.
7. Kittel, C., *Introduction to Solid State Physics.* Wiley: India, 2011.
8. Arblaster, J. W., Crystallographic Properties of Platinum new methodology and erratum. *Platin. Met. Rev.* **2006**, *50*, 118-119.
9. Brownlee, L. D., Lattice Constant of Grey Tin. *Nature* **1950**, *166*, 482.
10. Thewlis, J.; Davey, A. R., Thermal Expansion of Grey Tin. *Nature* **1954**, *174*, 1011.
11. Jette, E. R.; Foote, F., Precision Determination of Lattice Constants. *J. Chem. Phys.* **1935**, *3*, 605-616.
12. Deshpande, V. T.; Sirdeshmukh, D. B., Thermal expansion of tetragonal tin. *Acta Crystallogr.* **1961**, *14*, 355-356.
13. Atrei, A.; Bardi, U.; Rovida, G.; Torrini, M.; Zanazzi, E.; Ross, P. N., Structure of the (001)- and (111)-oriented surfaces of the ordered fcc $Pt_3Sn$ alloy by low-energy-electron-diffraction intensity analysis. *Phys. Rev. B* **1992**, *46*, 1649-1654.
14. Durussel, P.; Massara, R.; Feschotte, P., Le système binaire PtSn. *J. Alloys Compd.* **1994**, *215*, 175-179.